PHYSICAL REVIEW B **111**, 205115 (2025)

Detection of chiral spin fluctuations driven by frustration in Mott insulators

Kuan H. Hsu,[1,2] Chunjing Jia,[3] Emily Z. Zhang,[2,4] Daniel Jost,[2] Brian Moritz,[2]
Rudi Hackl,[5,6] and Thomas P. Devereaux[1,2,4,*]
[1]*Department of Materials Science and Engineering, Stanford University, California 94305, USA*
[2]*Stanford Institute for Materials and Energy Sciences, SLAC National Accelerator Laboratory,*
2575 Sand Hill Road, Menlo Park, California 94025, USA
[3]*Department of Physics, University of Florida, Florida 32611, USA*
[4]*Geballe Laboratory for Advanced Materials, Stanford University, California 94305, USA*
[5]*School of Natural Sciences, Technische Universität München, 85748 Garching, Germany*
[6]*IFW Dresden, Helmholtzstrasse 20, 01069 Dresden, Germany*

(Received 13 February 2025; accepted 30 April 2025; published 12 May 2025)

Topologically ordered states, such as chiral spin liquids, have been proposed as candidates that host fractionalized excitations. However, detecting chiral character or proximity to these nontrivial states remains a challenge. Resonant Raman scattering can be a powerful tool for detecting chiral fluctuations, as the A_{2g} channel probes excitations with broken time-reversal symmetry and local chiral order. Here, we use exact diagonalization to characterize the resonant A_{2g} channel, alongside two-magnon scattering in B_{1g} and E_g channels, for the Hubbard model on lattices with increasing levels of geometric spin frustration, where tuning the incident energy near the Mott gap reveals strong chiral spin excitation intensity. Increased spin frustration in the Mott insulator results in an overall softening of the Raman A_{2g} response, indicating a tendency toward low energy chiral-chiral fluctuations in Mott insulators with magnetic frustration and proximity to chiral spin liquid states that can potentially be tuned by external perturbations.

DOI: 10.1103/PhysRevB.111.205115

I. INTRODUCTION

In strongly correlated systems, frustration can give rise to exotic phases such as quantum spin liquids (QSL), a highly entangled state that lacks magnetic ordering even down to zero temperature [1,2]. A subclass of QSLs, known as chiral spin liquids (CSL), can host fractionalized quasiparticle excitations with non-Abelian statistics, giving rise to unusual phenomena such as the fractional quantum Hall effect [3], and unconventional superconductivity [4,5]. These states, which break both parity and time-reversal symmetry, may occur even in systems whose parent Hamiltonians are time-reversal invariant (Kalmeyer-Laughlin type). For example, theoretical and numerical studies suggest that such CSLs may be realized in geometrically frustrated Hubbard-type models [6–11].

Experimentally detecting CSLs remains challenging, as there are no direct probes for their fractionalized excitations. However, one can measure the scalar spin chirality (SSC), offering an avenue for detecting unusual spin textures and time-reversal symmetry breaking fluctuations in frustrated magnets. For instance, a nonvanishing SSC in a spin liquid phase can be a useful indicator to determine whether or not a QSL is chiral. In magnetically ordered ground states from $SU(2)$ symmetric systems, signatures of low lying excited states with chiral character can also serve as an indication that a CSL state may lie in close proximity of the ground state. Such states could potentially be stabilized with external perturbations. Nevertheless, detecting SSC both experimentally and theoretically have been less explored as a tool for identifying chiral character in putative QSL states.

To date, several experimental techniques for detecting SSC in magnetic systems have been proposed. Shastry and Shraiman first pointed out that fluctuations of the SSC operator couple to the A_{2g} channel in Raman scattering on a square lattice geometry [12,13]. Resonant inelastic scattering (RIXS) in the pre-edge region, with a dipole excitation of a core electron to an off-site valence orbital, has also been proposed as a means to measure SSC [14]; however, the use of high-energy x-rays limits the experimental resolution. Neutron scattering also may be able to detect SSC if the chiral spin fluctuations couple to S_z fluctuations [15].

Even with these proposals, Raman spectroscopy remains the only realized experimental technique that directly detects chiral spin fluctuations. As an optical probe, Raman scattering also allows for smaller sample sizes, making it easily accessible for single-crystal and thin-film experiments [16]. Although limited to providing information for very small momentum transfer, Raman scattering serves as a well-established technique for analyzing dynamical properties by selectively utilizing photon polarization to project out the symmetry group of excited states. Measurements of the A_{2g} channel have been made in insulating cuprates [17–19], a kagome spin liquid candidate [20], and a heavy fermion superconductor [21].

In this paper, we study the Raman scattering cross-section of the two-dimensional Hubbard model at half-filling. We calculate the resonant Raman cross-section directly by

---

[*] Contact author: tpd@stanford.edu

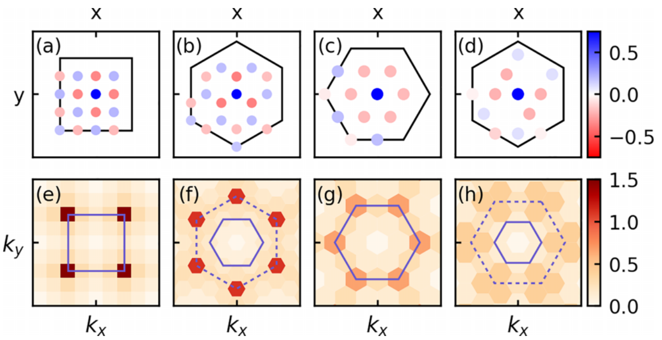

FIG. 1. Real space spin-spin correlation $\mathbf{S_r}$ (a)–(d) and static spin structure factor $\mathbf{S_q^{zz}}$ (e)–(h) in the strong coupling limit: Unit cells in the first row for the (a) 4 × 4 square lattice, (b) 3 × 3 honeycomb lattice, (c) 12 site (12C [24]) triangular lattice, and (d) 2 × 2 kagome lattice are shown with the real space spin-spin correlation S_r plotted as colored dots for points inside the unit cell. The corresponding first (extended) Brillouin zones are plotted in the second row for each lattice type using solid (dashed) blue lines. The intensity of the static spin structure factor S_q^{zz} is plotted for the accessible k-points in each panel. The spin structure factor calculated using either the Hubbard model with $U = 40t$ or the Heisenberg model provide consistent results.

using exact diagonalization (ED) and perturbation theory for the light-matter interaction (Fermi's Golden Rule) [22]. Specifically, we focus on Raman scattering in the A_{2g} channel, which probes excited states that break time-reversal symmetry. The dynamical properties of the Hubbard model are modified by tuning the frustration with different lattice geometries, with increasing spin frustration from the square and honeycomb lattices to the triangular and kagome lattices. Frustration is also introduced by decreasing the strength of Coulomb interaction strength in the Hubbard model, rather than relying exclusively on a down-folded, spin-only Heisenberg picture.

We first study the static spin correlations, showing that the static spin structure factor becomes increasingly incoherent with greater geometric frustration and weaker electron correlation. We derive and calculate the Raman A_{2g} response in the Heisenberg limit as a chiral-chiral correlator, which smoothly connects to the Raman A_{2g} cross-section calculated for the Hubbard model in the off-resonance regime. We observe a softening of the Raman response in both the two-magnon and the A_{2g} scattering channel when the ground state appears to be in close proximity to a nascent chiral spin state for highly frustrated lattice geometries, which may be stabilized by external fields [23]. When the incident energy is tuned near resonance, we show that the Raman A_{2g} cross section is significantly enhanced and can serve as a reliable tool to detect chiral character in potential CSL candidates.

II. RESULTS

A. Spin structure factor

We first consider the spin structure factor S_q for the Hubbard model on four lattices in Fig. 1. The real space spin-spin correlations in S_r for the square lattice show that spins are aligned antiferromagnetically, with the corresponding momentum-space S_q strongly peaked at the M-point $[(\pi,\pi)]$ in the Brillouin zone [see Figs. 1(a) and 1(e)]. Here, antiferromagnetism persists for all values of U.

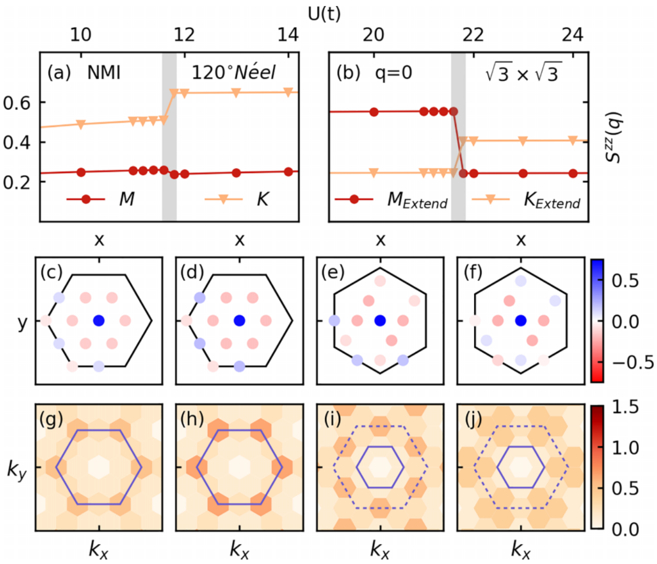

FIG. 2. Changes in the ground states on the (a) triangular and (b) kagome lattice, characterized by real space spin-spin correlation $\mathbf{S_r}$, and static spin structure factor $\mathbf{S_q^{zz}}$: Sharp changes in the static spin structure factor at the K and M points in the (extended for kagome lattice) Brillouin zone near ground state transitions are shown across various values of U. The shaded area specifies the region where the ground state transition occurs. Real-space spin-spin correlations are displayed for (c) the triangular lattice in the NMI state at $U = 11t$, and (d) the 120° Néel state at $U = 12t$, with their respective static spin structure factors in panels (g) and (h). For the kagome lattice, real-space spin-spin correlations for the $q = 0$ state at $U = 21t$ and the $\sqrt{3} \times \sqrt{3}$ state at $U = 22t$ are shown in (e) and (f), with corresponding static spin structure factors in (i) and (j).

Similar to the square lattice, the honeycomb lattice is bipartite and possesses an antiferromagnetic ground state at large enough U. Here, we evaluate the Hubbard model on a 3 × 3 honeycomb lattice (18 total sites). In the strong coupling limit, the spins are aligned antiferromagnetically with S_q peaked at the K-point of the extended Brillouin zone [see Figs. 1(b) and 1(f)]. The strength of S_q gradually decreases with decreasing U, but the antiferromagnetic ordering persists until $U = 8t$ with no change in ground state characteristics.

Geometric frustration becomes significant on triangular lattices, where spin liquid phases have been proposed to be potential ground state candidates for frustrated magnets [25,26] and organic Mott insulators [27–29]. For a triangular lattice Hubbard model in the strong coupling limit, frustration leads to a 120° Néel state with long-range order and S_q peaked at the K-point of the Brillouin zone [see Figs. 1(c) and 1(g)], albeit less strongly than that of the honeycomb lattice.

Stronger charge fluctuations in the intermediate coupling regime can lead to an instability in the ground state where the long-range antiferromagnetic order disappears. At $U < 11.8t$, S_q at the K-point $[(\frac{4}{3}\pi,0)]$ shows a sharp decrease [Fig. 2(a)], signifying the destruction of 120° Néel order. Here, translational symmetry is broken and the ground state momentum shifts to the M-point, where the ground state becomes

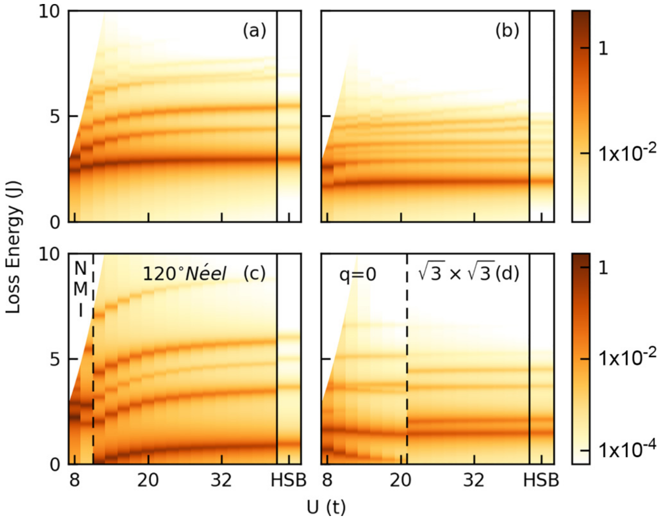

FIG. 3. Off-resonance Raman spectra for (a) $\mathbf{B_{1g}}$ square lattice (b) $\mathbf{E_g}$ honeycomb lattice (c) $\mathbf{E_g}$ triangular lattice and (d) $\mathbf{E_g}$ kagome lattices, with incident energy at $\omega_i = U/4$: The spectra are calculated as a function of U in the Hubbard model, while the right-most column in each panel with the label *HSB* is the Raman spectra calculated in the Heisenberg model using an effective Raman scattering operator evaluated for $U = 40t$. Ground state transitions as a function of U are highlighted by dashed lines, where the different ground states have been labeled for both the triangular and kagome lattices.

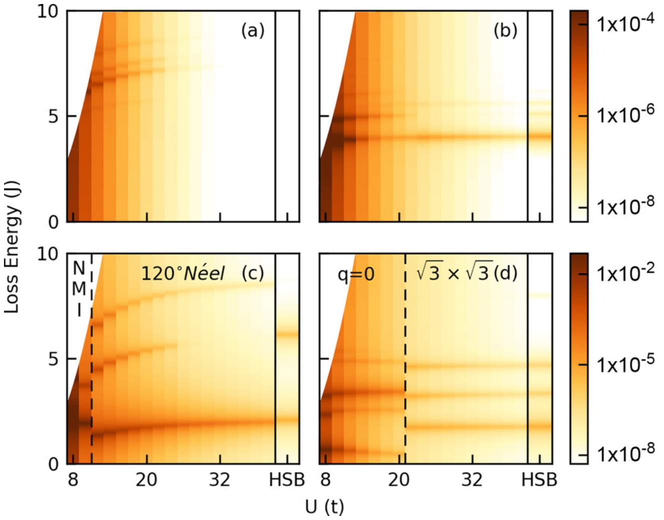

FIG. 4. Off-resonance Raman spectra in $\mathbf{A_{2g}}$ symmetry calculated for (a) square lattice, (b) honeycomb lattice, (c) triangular lattice, and (d) kagome lattices, with incident energy $\omega_i = U/4$: The calculated spectra plotted in this figure have the same layout and use the same broadening parameters as in Fig. 3. The intensity for Raman A_{2g} scattering on the square lattice (panel (a)) in the Heisenberg limit ($< 1 \times 10^{-10}$) is too small to appear on the plot for this intensity range.

nonmagnetically insulating (NMI). Here, the change from 120° Néel order to NMI is subtle and may be hard to observe without detailed inspection of the spin structure factor. Studies on large clusters have also indicated a ground state transition to a spin liquid candidate NMI state at similar values of U [11,30–32].

Electrons arranged on a kagome lattice experience the most geometric frustration. The kagome lattice consists of corner-sharing triangles where the spins on individual plaquettes are geometrically frustrated. At large U for the Hubbard model on a 2×2 kagome lattice (12 total sites), S_q possesses weak peaks near the K-points of the extended Brillouin zone [see Figs. 1(d) and 1(h)]. At intermediate coupling where $U < 21.8t$, S_q is more strongly peaked at the M-points [Figs. 2(e) and 2(i)]. This change in the spin correlations signifies a change of spin ordering at the ground state transition, going from a $\sqrt{3} \times \sqrt{3}$ ordered state to a $q = 0$ ordered state [33]. We note that a study with larger clusters also demonstrated a similar ground state transition behavior on a $2 \times \mathrm{L}$ kagome cylinder [34].

B. Resonant Raman scattering in the off-resonance regime

Raman light-scattering complements neutron scattering and can be used to understand the nature of spin excitations. Unlike neutron scattering that probes excitations involving odd numbers of spin-flips, Raman scattering enables the probing of even spin-flip excitations in a material that reflects the symmetry of the two dipole transitions compatible with the selected photon polarizations. Formally, Raman scattering can be decomposed into nonresonant, resonant, and mixed responses. Nonresonant scattering, or Thomson scattering, is a two-particle process that directly connects the initial and final states via the stress tensor operator and is only dependent on the energy transfer of the photon, whereas resonant Raman scattering is mediated through excitations to intermediate states via a four particle process [22].

In this section, we calculate the resonant Raman scattering cross-section off-resonance using two methods: (1) direct evaluation of the resonant Raman response in the Hubbard model using the Kramers-Heisenberg expression far away from resonance; and [22] (2) an effective Raman response in the Heisenberg model using the Shastry-Shraiman formulation [12,13], valid when U is much larger than the incident photon energy ω_i and nearest neighbor hopping t. Here, focus is placed on intermediate to strong coupling, where the spin and charge responses are well separated because of the Mott gap. Expressions for effective Raman scattering operators in spin language are provided in the Supplemental Material [35]. All figures in the results feature line-structures that smoothly connect the Raman response in the Hubbard model to that of the Heisenberg model in the large U limit. These structures correspond to different spin excitations with even number of spin flips that are symmetry selected by the polarizations; however, we primarily focus on the evolution of the lowest energy excitations without commenting specifically on their character.

We consider the half-filled Hubbard model having charge gaps, and therefore we limit focus on the most resonant diagrams only. We will consider these diagrams when the incident photon energy is tuned away from any direct transition (calling it ”off-resonance”) in this section, and in the following section we consider nearly ”on-resonant” scattering.

In all lattice geometries considered here, the A_{2g} symmetry channel projects to the antisymmetric part of the matrix element where the photon polarization is taken to be $e_x^f e_y^i - e_y^f e_x^i$, effectively probing states that break time-reversal symmetry. In the A_{2g} symmetry channel, the stress tensor cancels exactly, allowing the resonant A_{2g} Raman operator to be expressed as an SSC operator. This expression allows us to investigate the chiral character of strongly correlated system through resonant Raman scattering.

Results

We first study Raman scattering on a two-dimensional square-lattice Hubbard model, where the low-energy physics is closely related to insulating cuprates [36]. Here, we examine the Hubbard model across various coupling strengths while maintaining the same off-resonance condition (where $\omega_i = U/4$) across all values of U. In subsequent figures, the exchange energy J is taken as $4t^2/U$, with Lorentzian broadening in incident energy $\Gamma_{\text{in}} = 1t$ and in loss energy of $\Gamma_{\text{loss}} = 0.1J$ (the same for the Heisenberg model). In all figures, the white region at the left-side of each panel indicates where the loss energy is larger than the incident energy and therefore physically inaccessible.

Figure 3(a) shows the off-resonant Raman scattering for the square-lattice Hubbard model at half-filling. In the B_{1g} channel, we take the polarizations to be $e_x^f e_x^i - e_y^f e_y^i$ (same as the E_g channel in other lattice geometries), which probes the antiferromagnetic excitations via two-magnon processes [37–40]. Here, the intensity remains strong as the interaction strength increases, displaying a low energy peak at $\sim 3J$, corresponding to the two-magnon excitation energy. In contrast, Fig. 4(a) shows scattering in the A_{2g} channel, where the polarizations are taken to be $e_x^f e_y^i - e_y^f e_x^i$. The energy loss has a leading peak $\sim 5J$, gradually increasing to $\sim 6J$ at large U and the scattering intensity decays rapidly in this channel, as excited states with chiral character are well separated from the ground state. The rapidly decaying intensity results from high order spin flip processes, with the first nonzero contribution of the effective scattering operator occurring at the order of $t^6/(\omega_i - U)^5$ (see the Supplemental Material [35]).

For the honeycomb lattice, the two-magnon energy loss, as observed in the E_g channel [see Fig. 3(b)], is $\sim 1.8J$, corresponding to the energy cost of flipping neighboring spins. On the other hand, the effective Raman scattering operator in the A_{2g} channel is finite at order $t^4/(\omega_i - U)^3$ [41], leading to stronger scattering intensity in the Raman A_{2g} channel when compared with the square lattice. Indeed, Fig. 4(b) shows that the intensity in the A_{2g} channel decays much more slowly than for the square lattice, and the energy loss is $\sim 4J$ in the intermediate to strong coupling regime ($U > 10t$). The gradual increase in charge fluctuations due to reduced coordination in the honeycomb lattice leads to stronger A_{2g} scattering intensity and softening in the energy loss.

On the triangular lattice, frustration can lead to a spectral downshift of the magnon dispersion, detectable in the Raman E_g channel [42,43], as seen in Fig. 3(c). In the strong coupling limit with 120° Néel ordering, the leading excitation in the A_{2g} channel occurs $\sim 2J$ [Fig. 4(c)], lower than that of both the square and hexagonal lattices, a further indication of the influence of frustration in the system. With decreasing coupling strength, the Raman spectra in the effective Heisenberg model [44] connects smoothly to the calculated spectra in the Hubbard model. As U changes in the intermediate coupling regime, a ground state transition occurs between $U = 10t$ and $12t$, clearly indicated by a discontinuity in the Raman spectra in both the E_g and A_{2g} channels [Figs. 3 and 4(c)].

In Fig. 4(d), we show that the calculated Raman spectra for the kagome Heisenberg and Hubbard models in the strongly correlated limit have loss energies in the A_{2g} channel $\sim 2J$, similar to the triangular lattice. While the low-energy excitation is gapped, finite-size studies are needed to ascertain the size dependence of the low-energy excitations observed in the A_{2g} channel as debates remain on the magnetic ordering of the kagome Heisenberg model [45–47]. At the ground state transition where $U \sim 20t$, Raman scattering in the E_g [Fig. 3(d)] [Fig. 4(d)] channel becomes nearly gapless with a clear discontinuity in the spectral features, indicative of a ground state transition into the $q = 0$ state. We emphasize that low-energy excitations in the A_{2g} channel persist in the $q = 0$ state, indicating that the ground state of the kagome Hubbard model may lie in close proximity to a chiral spin liquid ground state.

C. Resonant Raman scattering near Mott gap

Often, the photon energy used in many Raman scattering experiments may lie near the value of U, far from the off-resonance regime. Additionally, some spin liquid candidate materials have been reported to have intermediate values of U [27,48]. In both cases, the Shastry-Shraiman approximation made in Sec. II B is no longer valid. Here, we calculate Raman scattering on resonance ($\omega_i = U$) to reveal strong chiral spin excitations that can be accessed when the incident energy is tuned near the upper Hubbard band center. Experimental measurements of cuprates also display enhancing intensity in A_{2g} channel when incident energy is on-resonance [19].

Figure 5 shows resonant Raman response in the B_{1g} and E_g symmetry for each lattice type. For the square and honeycomb lattices, the scattering amplitude is roughly an order of magnitude larger than off-resonance. The scattering intensity no longer decays with increasing U; instead, the intensities are on the same order of magnitude across all U, as high energy spin excitations become much more visible compared to off-resonance conditions. The overall characteristics of the excitation profile remain similar to that in the off-resonance regime (Fig. 3), as expected, since the character of the final states remain the same regardless of the resonant condition.

For the triangular lattice, the scattering amplitude in the E_g channel is noticeably stronger in the 120° Néel state than in the NMI state [Fig. 3(c)]. Similarly, the scattering amplitude in the E_g channel is also slightly stronger in the $q = 0$ state for the kagome lattice [Fig. 3(d)]. Here, the change in intensity of the two-magnon scattering is consistent with the result shown in the spin structure factor as discussed in Sec. II A.

Resonant Raman scattering in the A_{2g} symmetry channel shows increasing scattering intensity as a function of U in Fig. 6, in stark contrast to the off-resonance scattering, where the intensity decreases exponentially as U increases (Fig. 4). On the square lattice, we see an enhancement of chiral spin

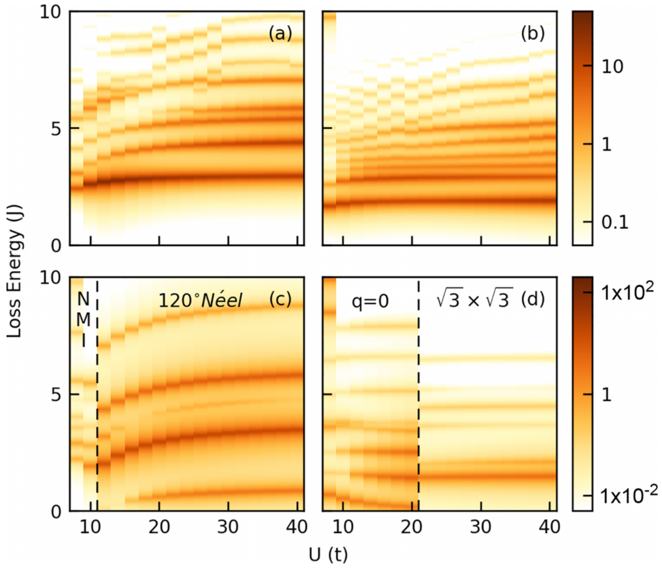

FIG. 5. Resonant Raman spectra in (a) $\mathbf{B_{1g}}$ square lattice, (b) $\mathbf{E_g}$ honeycomb lattice, (c) $\mathbf{E_g}$ triangular lattice, and (d) $\mathbf{E_g}$ kagome lattices, with incident energy at $\omega_i = U$: The calculated spectra plotted in this figure have the same layout and broadening parameters as in Fig. 3. The resonant Raman spectra exhibit a similar excitation profile to the off-resonance Raman spectra in Fig. 3. However, the peak amplitudes differ from those off-resonance, due to different processes.

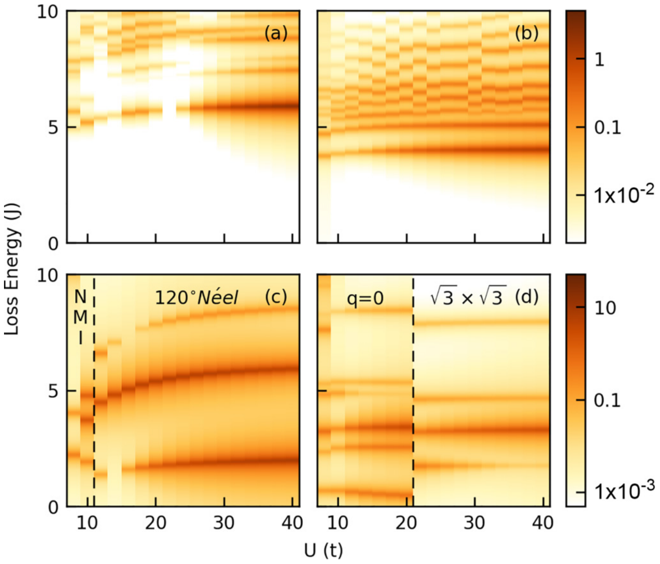

FIG. 6. Resonant Raman spectra in $\mathbf{A_{2g}}$ symmetry calculated for (a) square lattice, (b) honeycomb lattice, (c) triangular lattice, and (d) kagome lattices, with incident energy $\omega_i = U$: The calculated spectra plotted in this figure have the same layout and broadening parameters as Fig. 3, with the same photon polarization as in Fig. 4.

excitations [Fig. 6(a)] around $5J$, previously weak in the off-resonance regime. By tuning the incident energy near resonance, we recover leading chiral spin excitations that are difficult to detect off-resonance. We note that previous experimental Raman measurements of insulating cuprates [17,40] also display enhanced intensity in A_{2g} channel when the incident photon energy is on-resonance. Although we show in Sec. II B that the Raman scattering intensity in the A_{2g} channel diminishes quickly with the off-resonance condition, resonant Raman scattering can still be an effective probe of chiral spin excitations, amplified by the resonance effect.

A similar enhancement of the A_{2g} scattering intensity can also be seen in honeycomb and triangular lattices, where the scattering intensity is now only an order of magnitude smaller than that of the E_g channel across all values of U. More notably, the Raman cross section in the A_{2g} channel for the kagome lattice is of the same order of magnitude as the other channels, with low lying chiral spin excitations visible in the $q = 0$ state [Fig. 6(d)], similar to off-resonance Raman scattering [Fig. 4(d)]. Here, the enhanced scattering intensity in A_{2g} symmetry makes resonant Raman scattering a promising tool for probing the existence of spin liquids with chiral character in materials with a kagome lattice geometry, especially those with large values of U, such as in herbertsmithite-like compounds [49].

III. DISCUSSION

We have analyzed the spin structure factor and resonant Raman cross section for the Hubbard model on different lattice geometries. The spin structure factor shows diminishing characteristics of antiferromagnetism with increasing frustration. Furthermore, ground state ordering can change with decreasing coupling strength in frustrated geometries. Finally, we employed Raman scattering in different scattering channels to understand the change in underlying symmetry of the ground state and the development of chiral character with increased geometric and charge frustration.

In the strongly correlated limit and off-resonance, the Raman scattering operator in the A_{2g} channel can be expressed in terms of scalar spin chirality to reveal the presence of chiral spin excitations. We showed that the strength of chiral spin fluctuations is highly dependent on the lattice geometry. Bipartite lattices, such as the square and honeycomb lattices, have much weaker scattering in the A_{2g} symmetry channel compared to frustrated triangular and kagome lattices. We observed a softening of the energy in the A_{2g} Raman response for both frustrated lattice geometries at the boundary of the respective ground-state transitions, indicating the emergence of chiral character in the intermediate coupling regime, as also shown in large cluster studies [32,34]. Meanwhile, a clear discontinuity in the Raman spectra can be seen in all symmetry channels across the ground-state transition. For the kagome lattice, we observed a near-gapless excitation in the Raman A_{2g} channel at intermediate coupling strength ($U \sim 20t$), suggesting that a possible chiral spin liquid phase may be stabilized in the Hubbard model on the kagome lattice with an appropriate perturbation [23].

Although the Raman A_{2g} scattering intensity is typically small in the off-resonance regime, it can become comparable in magnitude to other scattering channels when the incident photon energy is tuned near resonance. Figure 6 clearly shows that the Raman A_{2g} scattering intensity increases to the same order of magnitude as the two-magnon response in other scattering channels on-resonance. Low-lying chiral spin excitations are accessible through the resonant processes when $\omega_{\text{in}} \sim U$ for all lattice geometries, allowing for reliable detection of chiral character in Mott insulators.

Our paper establishes the utility of Raman A_{2g} scattering for detecting chiral fluctuations in Mott insulators. However, a few open questions remain. Firstly, we note that finite-size effects are large in the small clusters considered in this paper, and we cannot directly capture the proposed spin liquid ground states in the triangular lattice Hubbard model in the intermediate coupling regime [11,29–32] or the kagome lattice Heisenberg models [46,47,50]. Numerical methods such as density matrix renormalization group (DMRG) allow for much larger cluster sizes, but it remains difficult to evaluate the resonant diagram using those techniques [51]. Nevertheless, we emphasize that Raman A_{2g} scattering effectively detects chiral character independent of finite-size effects, and opens an avenue for numerical studies on larger clusters and future experiments.

Additionally, we have only considered Raman scattering in Hubbard models with nearest-neighbor interactions. However, similar studies may be performed on more sophisticated models that can better describe different exotic phases, such as the inclusion of long-range interactions or antisymmetric exchange terms that introduce additional frustration beyond lattice geometry, which may also lead to the realization of a CSL phase. Without relying on an effective Raman scattering operator, one can compute and study the chiral spin excitations by evaluating the Kramers-Heisenberg formula for resonant Raman scattering in the A_{2g} channel to study the emergence of CSL states in frustrated Mott insulators.

ACKNOWLEDGMENTS

We thank T. Tang, J. K. Ding and M. Claassen for helpful discussions and suggestions. This paper was supported by the U.S. Department of Energy (DOE), Office of Basic Energy Sciences, Division of Materials Sciences and Engineering. Computation work was performed on the resources of the National Energy Research Scientific Computing Center (NERSC) supported by the U.S. Department of Energy, Office of Science, using NERSC Award No. BES-ERCAP0027203. C.J. acknowledges the support from Center for Molecular Magnetic Quantum Materials, an Energy Frontier Research Center funded by the U.S. Department of Energy, Office of Science, Basic Energy Sciences under Award No. DE-SC0019330.

DATA AVAILABILITY

The data supporting this study are available from the authors upon reasonable request.

[1] L. Balents, Spin liquids in frustrated magnets, Nature (London) **464**, 199 (2010).

[2] C. Broholm, R. J. Cava, S. A. Kivelson, D. G. Nocera, M. R. Norman, and T. Senthil, Quantum spin liquids, Science **367**, eaay0668 (2020).

[3] V. Kalmeyer and R. B. Laughlin, Theory of the spin liquid state of the Heisenberg antiferromagnet, Phys. Rev. B **39**, 11879 (1989).

[4] R. B. Laughlin and Z. Zou, Properties of the chiral-spin-liquid state, Phys. Rev. B **41**, 664 (1990).

[5] X. G. Wen, F. Wilczek, and A. Zee, Chiral spin states and superconductivity, Phys. Rev. B **39**, 11413 (1989).

[6] K. Yang, L. K. Warman, and S. M. Girvin, Possible spin-liquid states on the triangular and kagomé lattices, Phys. Rev. Lett. **70**, 2641 (1993).

[7] H. Yao and S. A. Kivelson, Exact chiral spin liquid with non-Abelian anyons, Phys. Rev. Lett. **99**, 247203 (2007).

[8] B. Bauer, L. Cincio, B. P. Keller, M. Dolfi, G. Vidal, S. Trebst, and A. W. W. Ludwig, Chiral spin liquid and emergent anyons in a kagome lattice Mott insulator, Nat. Commun. **5**, 5137 (2014).

[9] L. Messio, S. Bieri, C. Lhuillier, and B. Bernu, Chiral spin liquid on a kagome antiferromagnet induced by the Dzyaloshinskii-Moriya interaction, Phys. Rev. Lett. **118**, 267201 (2017).

[10] S.-S. Gong, W. Zheng, M. Lee, Y.-M. Lu, and D. N. Sheng, Chiral spin liquid with spinon Fermi surfaces in the spin-$\frac{1}{2}$ triangular Heisenberg model, Phys. Rev. B **100**, 241111 (2019).

[11] A. Szasz, J. Motruk, M. P. Zaletel, and J. E. Moore, Chiral spin liquid phase of the triangular lattice Hubbard model: A density matrix renormalization group study, Phys. Rev. X **10**, 021042 (2020).

[12] B. S. Shastry and B. I. Shraiman, Theory of Raman scattering in Mott-Hubbard systems, Phys. Rev. Lett. **65**, 1068 (1990).

[13] B. S. Shastry and B. I. Shraiman, Raman scattering in Mott-Hubbard systems, Int. J. Mod. Phys. B **05**, 365 (1991).

[14] W.-H. Ko and P. A. Lee, Proposal for detecting spin-chirality terms in Mott insulators via resonant inelastic x-ray scattering, Phys. Rev. B **84**, 125102 (2011).

[15] P. A. Lee and N. Nagaosa, Proposal to use neutron scattering to access scalar spin chirality fluctuations in kagome lattices, Phys. Rev. B **87**, 064423 (2013).

[16] D. Wulferding, Y. Choi, W. Lee, and K.-Y. Choi, Raman spectroscopic diagnostic of quantum spin liquids, J. Phys.: Condens. Matter **32**, 043001 (2020).

[17] P. E. Sulewski, P. A. Fleury, K. B. Lyons, and S.-W. Cheong, Observation of chiral spin fluctuations in insulating planar cuprates, Phys. Rev. Lett. **67**, 3864 (1991).

[18] R. Liu, D. Salamon, M. V. Klein, S. L. Cooper, W. C. Lee, S.-W. Cheong, and D. M. Ginsberg, Novel Raman-active electronic excitations near the charge-transfer gap in insulating cuprates, Phys. Rev. Lett. **71**, 3709 (1993).

[19] N. Chelwani, A. Baum, T. Böhm, M. Opel, F. Venturini, L. Tassini, A. Erb, H. Berger, L. Forró, and R. Hackl, Magnetic excitations and amplitude fluctuations in insulating cuprates, Phys. Rev. B **97**, 024407 (2018).

[20] D. Wulferding, P. Lemmens, P. Scheib, J. Röder, P. Mendels, S. Chu, T. Han, and Y. S. Lee, Interplay of thermal and quantum spin fluctuations in the kagome lattice compound herbertsmithite, Phys. Rev. B **82**, 144412 (2010).

[21] H.-H. Kung, R. E. Baumbach, E. D. Bauer, V. K. Thorsmølle, W.-L. Zhang, K. Haule, J. A. Mydosh, and G. Blumberg, Chirality density wave of the "hidden order" phase in $\mathrm{URu_2Si_2}$, Science **347**, 1339 (2015).

[22] T. P. Devereaux and R. Hackl, Inelastic light scattering from correlated electrons, Rev. Mod. Phys. **79**, 175 (2007).

[23] M. Claassen, H.-C. Jiang, B. Moritz, and T. P. Devereaux, Dynamical time-reversal symmetry breaking and photo-induced chiral spin liquids in frustrated Mott insulators, Nat. Commun. **8**, 1192 (2017).

[24] D. D. Betts, H. Q. Lin, and J. S. Flynn, Improved finite-lattice estimates of the properties of two quantum spin models on the infinite square lattice, Can. J. Phys. **77**, 353 (1999).

[25] Y. Shen, Y.-D. Li, H. Wo, Y. Li, S. Shen, B. Pan, Q. Wang, H. C. Walker, P. Steffens, M. Boehm, Y. Hao, D. L. Quintero-Castro, L. W. Harriger, M. D. Frontzek, L. Hao, S. Meng, Q. Zhang, G. Chen, and J. Zhao, Evidence for a spinon Fermi surface in a triangular-lattice quantum-spin-liquid candidate, Nature (London) **540**, 559 (2016).

[26] H. D. Zhou, E. S. Choi, G. Li, L. Balicas, C. R. Wiebe, Y. Qiu, J. R. D. Copley, and J. S. Gardner, Spin liquid state in the $s = 1/2$ triangular lattice $\mathrm{Ba_3CuSb_2O_9}$, Phys. Rev. Lett. **106**, 147204 (2011).

[27] Y. Shimizu, K. Miyagawa, K. Kanoda, M. Maesato, and G. Saito, Spin liquid state in an organic Mott insulator with a triangular lattice, Phys. Rev. Lett. **91**, 107001 (2003).

[28] K. Kanoda and R. Kato, Mott physics in organic conductors with triangular lattices, Annu. Rev. Condens. Matter Phys. **2**, 167 (2011).

[29] R. V. Mishmash, J. R. Garrison, S. Bieri, and C. Xu, Theory of a competitive spin liquid state for weak Mott insulators on the triangular lattice, Phys. Rev. Lett. **111**, 157203 (2013).

[30] T. Shirakawa, T. Tohyama, J. Kokalj, S. Sota, and S. Yunoki, Ground-state phase diagram of the triangular lattice Hubbard model by the density-matrix renormalization group method, Phys. Rev. B **96**, 205130 (2017).

[31] B.-B. Chen, Z. Chen, S.-S. Gong, D. N. Sheng, W. Li, and A. Weichselbaum, Quantum spin liquid with emergent chiral order in the triangular-lattice Hubbard model, Phys. Rev. B **106**, 094420 (2022).

[32] J.-S. Xu, Z. Zhu, K. Wu, and Z.-Y. Weng, Hubbard model on a triangular lattice: The role of charge fluctuations, Phys. Rev. B **109**, L081116 (2024).

[33] L. Messio, C. Lhuillier, and G. Misguich, Lattice symmetries and regular magnetic orders in classical frustrated antiferromagnets, Phys. Rev. B **83**, 184401 (2011).

[34] R.-Y. Sun and Z. Zhu, Metal-insulator transition and intermediate phases in the kagome lattice Hubbard model, Phys. Rev. B **104**, L121118 (2021).

[35] See Supplemental Material at http://link.aps.org/supplemental/10.1103/PhysRevB.111.205115 for derivation of effective Raman scattering operator in A_{2g} symmetry on square lattice.

[36] F. C. Zhang and T. M. Rice, Effective Hamiltonian for the superconducting Cu oxides, Phys. Rev. B **37**, 3759 (1988).

[37] P. A. Fleury and R. Loudon, Scattering of light by one- and two-magnon excitations, Phys. Rev. **166**, 514 (1968).

[38] G. Blumberg, P. Abbamonte, M. V. Klein, W. C. Lee, D. M. Ginsberg, L. L. Miller, and A. Zibold, Resonant two-magnon Raman scattering in cuprate antiferromagnetic insulators, Phys. Rev. B **53**, R11930 (1996).

[39] A. V. Chubukov and D. M. Frenkel, Resonant two-magnon Raman scattering in antiferromagnetic insulators, Phys. Rev. Lett. **74**, 3057 (1995).

[40] B. Muschler, W. Prestel, L. Tassini, R. Hackl, M. Lambacher, A. Erb, S. Komiya, Y. Ando, D. C. Peets, W. N. Hardy, R. Liang, and D. A. Bonn, Electron interactions and charge ordering in $\mathrm{CuO_2}$ compounds, Eur. Phys. J.: Spec. Top. **188**, 131 (2010).

[41] W.-H. Ko, Z.-X. Liu, T.-K. Ng, and P. A. Lee, Raman signature of the U(1) Dirac spin-liquid state in the spin-$\frac{1}{2}$ kagome system, Phys. Rev. B **81**, 024414 (2010).

[42] W. Zheng, J. O. Fjærestad, R. R. P. Singh, R. H. McKenzie, and R. Coldea, Anomalous excitation spectra of frustrated quantum antiferromagnets, Phys. Rev. Lett. **96**, 057201 (2006).

[43] F. Vernay, T. P. Devereaux, and M. J. P. Gingras, Raman scattering for triangular lattices spin-1/2 Heisenberg antiferromagnets, J. Phys.: Condens. Matter **19**, 145243 (2007).

[44] T. Tang, B. Moritz, and T. P. Devereaux, Spectra of a gapped quantum spin liquid with a strong chiral excitation on the triangular lattice, Phys. Rev. B **106**, 064428 (2022).

[45] R. R. P. Singh and D. A. Huse, Triplet and singlet excitations in the valence bond crystal phase of the kagome lattice Heisenberg model, Phys. Rev. B **77**, 144415 (2008).

[46] Y. Ran, M. Hermele, P. A. Lee, and X.-G. Wen, Projected-wave-function study of the spin-1/2 Heisenberg model on the kagomé lattice, Phys. Rev. Lett. **98**, 117205 (2007).

[47] S. Yan, D. A. Huse, and S. R. White, Spin-liquid ground state of the s = 1/2 kagome Heisenberg antiferromagnet, Science **332**, 1173 (2011).

[48] A. K. McMahan, J. F. Annett, and R. M. Martin, Cuprate parameters from numerical Wannier functions, Phys. Rev. B **42**, 6268 (1990).

[49] H. O. Jeschke, F. Salvat-Pujol, and R. Valentí, First-principles determination of Heisenberg Hamiltonian parameters for the spin-$\frac{1}{2}$ kagome antiferromagnet $\mathrm{ZnCu_3(OH)_6Cl_2}$, Phys. Rev. B **88**, 075106 (2013).

[50] S. Bieri, C. Lhuillier, and L. Messio, Projective symmetry group classification of chiral spin liquids, Phys. Rev. B **93**, 094437 (2016).

[51] A. Nocera, U. Kumar, N. Kaushal, G. Alvarez, E. Dagotto, and S. Johnston, Computing resonant inelastic x-ray scattering spectra using the density matrix renormalization group method, Sci. Rep. **8**, 11080 (2018).